

Cosmological implication of cross-correlation between galaxy clustering and 21-cm line intensity mapping

YONG-SEON SONG,¹ MINJI OH,² KYUNGJIN AHN,³ AND FENG SHI⁴

¹*Korea Astronomy and Space Science Institute, Daejeon 34055, Republic of Korea; ysong@kasi.re.kr*

²*Department of Earth Sciences, Chosun University, Gwangju 61452, Republic of Korea*

³*Department of Earth Sciences, Chosun University, Gwangju 61452, Republic of Korea; kjahn@chosun.ac.kr*

⁴*School of Aerospace Science and Technology, Xidian University, Xi'an, 710126, China*

ABSTRACT

The apparent anisotropies of galaxy clustering and 21-cm mapping in redshift space offer a unique opportunity to simultaneously probe cosmic expansion and gravity on cosmological scales through the Alcock–Paczynski (AP) effect and redshift-space distortions (RSD). Although improved theoretical models exist for anisotropic clustering, their applicability is limited by the non-perturbative smearing effect caused by the randomness of relative velocities. Here, we consider an alternative approach using the statistical power of cross-correlation between galaxy clustering and 21-cm line intensity mapping. Based on Fisher matrix analysis, fully incorporating nonlinear RSD, we estimate the benefit of combining both observables. We find that, for spectroscopy surveys like DESI combined with 21-cm line-intensity mapping surveys, the constraint on the growth of structure is improved by a factor of two relative to the galaxy auto-correlation, while the constraint on the cosmic expansion is only slightly improved. Crucially, such an observation can strongly constrain the neutral hydrogen (HI) content Ω_{HI} to a sub-percent level. This level of precision unlocks the potential of this method to probe post-reionization astrophysics with enhanced precision. It would far surpass existing constraints from stacked 21-cm emission (resulting in $\sim 50\% - 100\%$ uncertainties) and break the degeneracy between Ω_{HI} and the HI bias b_{HI} inherent in linear-regime power spectrum analysis. This cross-correlation approach effectively compensates for the loss of constraining power when using galaxy clustering alone.

Keywords: large-scale structure formation, 21cm intensity mapping, radio cosmology, galaxy survey

1. INTRODUCTION

In our current understanding of the universe, an unknown substance called dark matter dominates over the standard model particles at the present epoch. Despite many theoretical and observational efforts, the origin of dark matter is not yet clarified. Also, the existence of dark energy, which is supposed to drive the cosmic acceleration, indicates our incomplete understanding of the gravity on cosmological scales. It may imply modifications to Einstein’s theory of General Relativity. A further insight into the origin and nature of dark energy or validity of general relativity is essential, and this is one of the primary goals in next-generation cosmology.

The large-scale structure offers an opportunity to probe these issues by looking at the anisotropic galaxy

clustering in redshift space. The observed galaxy distribution via the spectroscopic measurements is apparently distorted due to the peculiar velocity of galaxies along the line-of-sight direction, referred to as the redshift-space distortions (RSD). While the RSD complicates the interpretation of the small-scale galaxy clustering, on large scales, the strength of anisotropies is simply characterized by the linear growth rate $f = d \ln G_\delta / d \ln a$, providing us a unique opportunity to probe the growth of structure, where G_δ and a are the density growth function and scale factor of the Universe, respectively. On the other hand, the large-scale galaxy clustering data imprints a fossil record of the primeval baryon-photon fluid around the last-scattering surface, known as the baryon acoustic oscillations (BAO). The characteristic scale of the BAO can be used as a standard ruler, which enables us to determine the geometric distances of high- z galaxies with greater precision. The key point to deter-

mine the geometric distances is to measure the clustering anisotropies over the BAO scales. Notice the fact that the anisotropies of the clustering pattern also arises from the apparent mismatch of the underlying cosmological model when we convert the redshift and angular position of each galaxy to the co-moving radial and transverse distances. This is the so-called Alcock-Paczynski (AP) effect, and with a prior knowledge of the characteristic scale of the BAO, the Hubble parameter $H(z)$ and angular diameter distance $D_A(z)$ of the high- z galaxies can be separately measured. Thus, the anisotropic galaxy clustering can serve as a dual cosmological probe from which we can explore the origin of cosmic acceleration from the viewpoint of both dark energy and modification of gravity. A recent claim that the flat wCDM model prefers the dark energy equation of state $w \neq -1$ comes from both the measure of BAO (Adame et al. 2025) and the AP test (Dong et al. 2023), showing the importance of these effects in cosmology.

To simultaneously constrain cosmic expansion and structure growth, a detailed theoretical model of anisotropic clustering is essential. Although our focus is near the linear regime, small, non-negligible nonlinear systematics, including gravitational clustering, must be corrected. Perturbation theory is a popular template for this correction beyond linear theory, but its applicability is limited to the weakly nonlinear regime. Furthermore, RSD introduces non-trivial crosstalk between scales. Specifically, the Finger-of-God (FoG) effect, caused by the virialized random motion of galaxies within halos, significantly suppresses the clustering amplitude along the line of sight, even on large scales. Since perturbation theory cannot fully describe the FoG effect, a phenomenological description must be introduced. Consequently, to avoid systematics, cosmological data analysis is restricted to large scales ($k \lesssim 0.1 h \text{ Mpc}^{-1}$), which severely reduces the statistical power to constrain cosmology.

In the pursuit of extracting maximal cosmological information exploiting the benefit of cross-correlation between galaxy clustering and 21-cm line intensity mapping (LIM), we present the combined results of the galaxy survey and 21-cm experiment to constrain the geometric distances and growth of structure. To be specific, we consider an accessible spectroscopic survey like Dark Energy Spectroscopic Instrument (hereafter DESI), which would be the best suited to probe the cosmic acceleration around $z \sim 1$. Considering this survey setup, we discuss the impact of the FoG effect on the estimation of cosmological parameters, which has not been explored to the nonlinear order as far as we know. We show that while the uncertainty of the FoG effect

in power spectrum is mostly degenerate with the coherent motion as a probe of the growth of structure, the combination of both power spectra breaks this degeneracy, thus improving the measurement accuracy of the coherent motion by a factor of two at most. As for the constraints on geometric distances, substantial improvement is not found.

Another benefit of our nonlinear formalism for the RSD in the cross-power spectrum is a potential to estimate the global hydrogen content, $\Omega_{\text{HI}} \equiv \rho_{\text{HI}}/\rho_{\text{crit}}$ to a very high accuracy as we will show. 21-cm observations so far do not yet seem to have reached sensitivity high enough to measure Ω_{HI} to a high accuracy. Constraints on Ω_{HI} at $z \lesssim 1$ come mainly from two categories of observations: (1) stacked signal of 21-cm emission lines from individual galaxies (Delhaize et al. 2013; Rhee et al. 2013, 2018; Tramonte & Ma 2020; Chen et al. 2021) and (2) the clustering properties (e.g. power spectrum) of 21-cm line intensity maps (Pen et al. 2009; Chang et al. 2010; Masui et al. 2013; Anderson et al. 2018; Li et al. 2021; Wolz et al. 2022; Amiri et al. 2023; Cunningham et al. 2022; CHIME Collaboration et al. 2025). For example, DINGO-VLA (Deep Investigations of Neutral Gas Origins–Very Large Array) team stacked 21-cm emission signals from thousands of galaxies, and have obtained $\Omega_{\text{HI}}(z = 0.05) = (0.38 \pm 0.04) \times 10^{-3}$ (Chen et al. 2021). Even though the $1-\sigma$ uncertainty is small, the theoretical uncertainty and the cosmic variance surpass the given uncertainty because the selection bias (only bright galaxies) may miss the contribution from faint galaxies and the sky coverage is still too small ($\sim 20 \text{ deg}^2$) to guarantee the mitigation of the cosmic variance. Canadian Hydrogen Intensity Mapping Experiment (CHIME) stacked 21-cm emission signals from individual objects but intentionally including nearly objects as well, to yield an estimate of the HI clustering property: $A_{\text{HI}}(z = 0.84) \equiv 10^3 \Omega_{\text{HI}} (b_{\text{HI}} + \langle f \mu^2 \rangle) = 1.51_{-0.97}^{+3.60}$ for Luminous Red Galaxy (LRG), $A_{\text{HI}}(z = 0.96) = 6.76_{-3.79}^{+9.04}$ for Emission Line Galaxy (ELG), and $A_{\text{HI}}(z = 1.20) = 1.68_{-0.67}^{+1.10}$ for QSOs, showing the dependence of A_{HI} on the type of galaxies (Amiri et al. 2023).

We will show that the usual degeneracy in estimation of Ω_{HI} and b_{HI} , shown in the clustering analysis by e.g. CHIME (Amiri et al. 2023; see also the one by MeerKAT+WiggleZ: Cunningham et al. 2022), can be broken by our formalism. While the full compilation of CHIME data may enable the estimation of the cross power spectrum with galaxy survey data, the standard linear-regime assumption in power spectrum analysis is insufficient to break the degeneracy between

Ω_{HI} and the HI bias b_{HI} . Furthermore, although a recent study (CHIME Collaboration et al. 2025) successfully reported the first highly significant detection of the HI auto power spectrum (yielding $A_{\text{HI}}(z = 1.16) = 2.59^{+1.26}_{-0.78}(\text{stat.})^{+2.45}_{-0.47}(\text{sys.})$), their methodology excludes data at $k < 0.4 \text{ h/Mpc}$ presumably due to foreground avoidance (a scheme to exclude k values that is most prone to the spectrally smooth foreground). The largeness of k in such cases requires a more sophisticated theoretical treatment to model the non-linear regime. Our formalism presented in this paper focusing on the quasi-linear regime $k \lesssim 0.1 \text{ h}^{-1} \text{ Mpc}$ at $z \sim 1$, if realized through observations, is expected to provide a much more accurate estimate of Ω_{HI} than these studies and thus improve its measurement significantly (Sec. 3.3), with the degeneracy between Ω_{HI} and b_{HI} broken.

This paper is organized as follows. In Section 2, we lay out a general formalism for auto- and cross-correlation power spectrums of the galaxy survey and the 21-cm LIM, but with a careful treatment of RSD extended to the non-linear regime. In Section 3, we show the expected constraints of cosmological and astrophysical parameters from our Fisher matrix analysis, focusing on the improved constraint on dynamics-related cosmological parameters and Ω_{HI} . In Section 4, we discuss the prospect of our methodology.

2. METHODOLOGY

2.1. The power spectrum in redshift space

The anisotropic power spectrum in redshift space is given as

$$P_{ab}(k, \mu) = \mathcal{C}_a \mathcal{C}_b \int d^3 \mathbf{x} e^{i \mathbf{k} \cdot \mathbf{x}} \langle e^{j_1 A_1} A_2^a A_3^b \rangle, \quad (1)$$

where a and b denote either the galaxy g or the hydrogen line H, and $\mathcal{C}_g = 1$ and $\mathcal{C}_H = p_S$. p_S is the power received by the antenna in the frequency bandwidth Δf (Seo et al. 2010):

$$p_S = p_S(z) = k_B \hat{T}_{\text{sig}} \Delta f \quad (2)$$

where the sky-averaged, observed temperature of the 21-cm background originating from the redshift z^1 , \hat{T}_{sig} , is given by

$$\hat{T}_{\text{sig}}(z) = 188 \frac{x_{\text{HI}} \Omega_{H,0} (1+z)^2 h}{H(z)/H_0} \text{ mK} \quad (3)$$

where $\Omega_{H,0} = X \Omega_{b,0} = 0.03753$, and x_{HI} is assumed to be unknown with a fiducial value $x_{\text{HI}} = 0.027$. This

value of x_{HI} is to reflect the fact that values deduced via the Lyman-alpha forest observation range from $\Omega_{\text{HI}}(z) \equiv x_{\text{HI}}(z) \Omega_{H,0} = (0.7 \pm 0.3) \times 10^{-3}$ (Rao et al. 2006) to $\Omega_{\text{HI}}(z) = (1.2 \pm 0.3) \times 10^{-3}$ (Grasha et al. 2020) at $z \simeq 1$. We set $P_{\epsilon_H \epsilon_H} = 100 \text{ h}^{-3} \text{ Mpc}^3$ (HI shot noise, to be defined in Eq. 15), which is based on the Schechter function fit to the hydrogen mass function (Zwaan et al. 2005).

The mapping between real space \mathbf{r} and redshift space \mathbf{s} is related as,

$$\mathbf{s} = \mathbf{r} + \frac{\mathbf{v} \cdot \hat{\mathbf{z}}}{aH} \hat{\mathbf{z}}, \quad (4)$$

where \mathbf{v} , a and H represent the peculiar velocity, the scale factor of the expansion, and the Hubble parameter respectively. The redshift distortion effect (hereafter RSD) is exhibited in this power spectrum formulation. The observer is assumed to be located far away from the targeted galaxies, in which the z -direction is effectively consistent with the line of sight direction. μ is the cosine of the angle between \mathbf{k} and the line of sight. The variable j_1 and functions A_i in Eq. (1) are defined,

$$\begin{aligned} j_1 &= -i k \mu, \\ A_1 &= u_z(\mathbf{r}) - u_z(\mathbf{r}'), \\ A_2^a &= [\delta_a(\mathbf{r}) + \nabla_z u_z(\mathbf{r})], \\ A_3^a &= [\delta_a(\mathbf{r}') + \nabla_z u_z(\mathbf{r}')]. \end{aligned} \quad (5)$$

The quantities \mathbf{x} and \mathbf{u} are given respectively by $\mathbf{x} = \mathbf{r} - \mathbf{r}'$ and $\mathbf{u} \equiv -\mathbf{v}/(aH)$. The function u_z is the line-of-sight component of \mathbf{u} . The density contrast of a tracer a is given by $\delta_a = b_a \delta_m$ with the tracer-specific bias b_a and the matter density contrast δ_m . Here we adopt the equivalence principle that the velocities are consistent among different tracers. The velocity fields are assumed to be those after correcting the possible density bias, as the surveys of presumed velocity fields are in fact probing the momentum fields (Appleby et al. 2023) and thus affected by the density bias.

The full expression of RSD power spectrum is split into perturbative and non-perturbative terms for practical purpose. In the quasi non-linear regime, Gaussian statistics are applied to expand both density and velocity fluctuations which exhibit infinite series of perturbative expansions. The non-perturbative part containing velocity terms is assumed to be separable, and the leading order follows to a simple exponential function dubbed by Finger of God (hereafter FoG). The full anisotropic power spectrum (Eq. 1) is expressed in leading orders as

$$P_{ab}(k, \mu) = \mathcal{C}_a \mathcal{C}_b D^{\text{FoG}}(k \mu \sigma_p) [P_{\delta_a \delta_b}(k)$$

¹ The observing frequency f is related to z implicitly by $f = 1.42/(1+z)$ GHz

$$+\mu^2 P_{\delta_a\Theta}(k) + \mu^2 P_{\delta_b\Theta}(k) + \mu^4 P_{\Theta\Theta}(k) + A_{ab}(k, \mu) \\ + B_{ab}(k, \mu) + T_{ab}(k, \mu) + F_{ab}(k, \mu)\Big], \quad (6)$$

where $\Theta \equiv -\nabla \cdot \mathbf{v}/(aH) = \nabla \cdot \mathbf{u}$, and σ_p is the line-of-sight velocity variance $\langle u_z^2 \rangle_c$ that we take as a free parameter in this paper. The spectra $P_{\delta_a\delta_b}$, $P_{\Theta\Theta}$, $P_{\delta_a\Theta}$, and $P_{\delta_b\Theta}$ are respectively the auto-power spectrum of density, velocity-divergence fields, and their cross-power spectrum, which are from $\langle A_2 A_3 \rangle_c$ under the assumption of the irrotational flow and form linear terms. $\langle F_1 F_2 \dots F_n \rangle_c$ is the connected average of quantities $\{F_1, F_2, \dots, F_n\}$. For more details of the terms and formalism, see Section 2.1 of [Song et al. \(2018\)](#)².

Nonlinear terms in Eq. (6), to the leading order, are composed of density and velocity terms (Eq. 5) and given by

$$A_{ab}(k, \mu) = j_1 \int d^3 \mathbf{x} e^{i\mathbf{k} \cdot \mathbf{x}} \langle A_1 A_2^a A_3^b \rangle_c, \\ B_{ab}(k, \mu) = j_1^2 \int d^3 \mathbf{x} e^{i\mathbf{k} \cdot \mathbf{x}} \langle A_1 A_2^a \rangle_c \langle A_1 A_3^b \rangle_c, \\ T_{ab}(k, \mu) = \frac{1}{2} j_1^2 \int d^3 \mathbf{x} e^{i\mathbf{k} \cdot \mathbf{x}} \langle A_2^2 A_2^a A_3^b \rangle_c, \\ F_{ab}(k, \mu) = -j_1^2 \int d^3 \mathbf{x} e^{i\mathbf{k} \cdot \mathbf{x}} \langle u_z u'_z \rangle_c \langle A_2^a A_3^b \rangle_c, \quad (7)$$

where $u_z(\mathbf{r})$ and $u_z(\mathbf{r}')$ are abbreviated as u_z and u'_z hereafter. Note that the factorized term D^{FoG} in Eq. (6) represents a non-perturbative contribution coming from the zero-lag correlation of velocity fields and plays a role in suppressing the overall amplitude at small scales.

The observed galaxy power spectrum in the weakly non-linear regime is expressed exploiting the perturbative formulation for the tracer field expansion containing matter density field δ , including the non-local contributions. Here, we adopt the prescription proposed by [McDonald & Roy \(2009\)](#) and [Saito et al. \(2014\)](#), which has been applied to the Baryon Oscillation Spectroscopic Survey (BOSS) in Sloan Digital Sky Survey (SDSS). Apart from the stochastic terms, this is a general perturbative expansion valid at the next-to-leading order. While the hybrid model for the matter power spectrum includes the corrections valid at next-to-next-to-leading order, we shall below consider the scales where the next-to-leading order is important, but the next-to-next-to-leading order is still subdominant.

2.2. Galaxy auto-correlation

² We have extended the original formalism by [Song et al. \(2018\)](#) into a double-tracer case, or the galaxy and the HI 21-cm, in Section 2.4 by employing the fact that A_1 (Eq. 5) is universal among different tracers.

The power spectrum of the galaxy tracer in real space is expressed as ([McDonald & Roy 2009](#); [Saito et al. 2014](#); [Gil-Marín et al. 2015](#)),

$$\tilde{P}_{\delta_g\delta_g}(k) = P_{\delta_g\delta_g}(k) + P_{\epsilon_g\epsilon_g}, \quad (8)$$

where the term $P_{\epsilon_g\epsilon_g}$ is the stochastic contribution mainly characterizing the shot noise, which is usually constant, and is estimated, assuming the Poisson noise, from the number density of tracer field.³ The first term, $P_{\delta_g\delta_g}$ in the right hand side, is the deterministic part, and is given by,

$$P_{\delta_g\delta_g}(k) = b_{g1}^2 P_{\delta\delta}(k) + 2b_{g1}b_{g2}P_{b2,\delta}(k) + 2b_{g1}b_{gs2}P_{bs2,\delta}(k) \\ + 2b_{g1}b_{g3\text{nl}}\sigma_3^2(k)P_m^L(k) + b_{g2}^2 P_{b22}(k) \\ + 2b_{g2}b_{gs2}P_{b2s2}(k) + b_{gs2}^2 P_{bs22}(k). \quad (9)$$

On the other hand, the cross-power spectrum, $P_{\delta_g\Theta}$, contains only the deterministic contribution, whose expression is given by $\tilde{P}_{\delta_g\Theta}(k) = P_{\delta_g\Theta}(k)$ where $P_{\delta_g\Theta}(k)$ is,

$$P_{\delta_g\Theta}(k) = b_{g1}P_{\delta\Theta}(k) + b_{g2}P_{b2,\Theta}(k) + b_{gs2}P_{bs2,\Theta}(k) \\ + b_{g3\text{nl}}\sigma_3^2(k)P_m^L(k). \quad (10)$$

Note that in the absence of velocity bias, the auto-power spectrum of galaxy velocity field is identical to $P_{\Theta\Theta}$. In Eqs. (9) and (10), while the first terms, $b_{g1}^2 P_{\delta\delta}$ and $b_{g1}P_{\delta\Theta}$, as well as $P_{\Theta\Theta}$, are the leading-order bias contribution, and can be computed with the hybrid RSD model for the matter power spectrum as described in Appendix A, the terms involving parameters b_{g2} , b_{gs2} , and $b_{g3\text{nl}}$ are the higher-order bias terms. The explicit expressions for their scale-dependent functions, $P_{b2,\delta}$, $P_{bs2,\delta}$, σ_3^2 , P_{b22} , P_{b2s2} , P_{bs22} , $P_{b2,\Theta}$ and $P_{bs2,\Theta}$ can be found in [Gil-Marín et al. \(2015\)](#) and [Saito et al. \(2014\)](#) and P_m^L is the linear matter power spectrum.

The A , B , T and F terms in Eq. (6) are all regarded as the higher-order corrections. Thus, we only apply the linear bias b_{g1} to these terms using Eqs. (7) and (5) and velocity biases are not assumed. First, $A_{gg}(k, \mu)$ can be estimated as

$$A_{gg}(k, \mu) = \sum_{n=1}^4 \mathcal{A}_{n,gg} \\ = (G_\delta/\bar{G}_\delta)^2 (G_\Theta/\bar{G}_\Theta) \bar{A}_{1,gg} + (G_\delta/\bar{G}_\delta) (G_\Theta/\bar{G}_\Theta)^2 \bar{A}_{2,gg} \\ + (G_\delta/\bar{G}_\delta) (G_\Theta/\bar{G}_\Theta)^2 \bar{A}_{3,gg} + (G_\Theta/\bar{G}_\Theta)^3 \bar{A}_{4,gg}, \quad (11)$$

where the barred quantities $\bar{A}_{n,gg}$ are measured in fiducial cosmology and they are rescaled to other cosmology

³ Throughout this paper, we denote the isotropic power spectrum inclusive of the stochasticity (noise) by \tilde{P} , to articulate its direct relevance to the observation.

using the growth functions G_δ and G_Θ defined in Appendix A. Note that $\bar{A}_{n,gg}$'s have an explicit dependence on b_{g1} except for $\bar{A}_{4,gg}$, as shown in Eq. (B9).

Similarly, $B_{gg}(k, \mu)$, $T_{gg}(k, \mu)$, and $F_{gg}(k, \mu)$ can be expressed as

$$\begin{aligned} B_{gg}(k, \mu) &= \sum_{n=1}^3 \mathcal{B}_{n,gg} \\ &= (G_\delta/\bar{G}_\delta)^2 (G_\Theta/\bar{G}_\Theta)^2 \bar{B}_{1,gg} + (G_\delta/\bar{G}_\delta) (G_\Theta/\bar{G}_\Theta)^3 \bar{B}_{2,gg} \\ &+ (G_\Theta/\bar{G}_\Theta)^4 \bar{B}_{3,gg}, \end{aligned} \quad (12)$$

$$\begin{aligned} T(k, \mu) &= \sum_{n=1}^7 \mathcal{T}_{n,gg} \\ &= (G_\delta/\bar{G}_\delta)^2 (G_\Theta/\bar{G}_\Theta)^2 \bar{T}_{1,gg} + (G_\delta/\bar{G}_\delta) (G_\Theta/\bar{G}_\Theta)^3 \bar{T}_{2,gg} \\ &+ (G_\delta/\bar{G}_\delta) (G_\Theta/\bar{G}_\Theta)^3 \bar{T}_{3,gg} + (G_\Theta/\bar{G}_\Theta)^4 \bar{T}_{4,gg} \\ &+ (G_\delta/\bar{G}_\delta)^2 (G_\Theta/\bar{G}_\Theta)^2 \bar{T}_{5,gg} + (G_\delta/\bar{G}_\delta) (G_\Theta/\bar{G}_\Theta)^3 \bar{T}_{6,gg} \\ &+ (G_\Theta/\bar{G}_\Theta)^4 \bar{T}_{7,gg}, \end{aligned} \quad (13)$$

and,

$$\begin{aligned} F(k, \mu) &= \sum_{n=1}^3 \mathcal{F}_{n,gg} \\ &= (G_\delta/\bar{G}_\delta)^2 (G_\Theta/\bar{G}_\Theta)^2 \bar{F}_{1,gg} + (G_\delta/\bar{G}_\delta) (G_\Theta/\bar{G}_\Theta)^3 \bar{F}_{2,gg} \\ &+ (G_\Theta/\bar{G}_\Theta)^4 \bar{F}_{3,gg}. \end{aligned} \quad (14)$$

The derivations of Eqs. (11-14) are described by Eqs. (B10), (B12), (B14) and (B16), respectively. The components $\bar{B}_{n,gg}$, $\bar{T}_{n,gg}$ and $\bar{F}_{n,gg}$ are derived in Eqs. (B11), (B13) and (B15), respectively. The accuracy of this treatment and its impacts on the RSD model are discussed in Zheng et al. (2019), and allows a rather accurate estimation of b_{g1} by breaking the degeneracy between b_{g1} and G_δ . This is due to the fact that our nonlinear formalism roughly encapsulates the power of the joint analysis of the linear power spectrum and the bi-spectrum suggested by Song et al. (2015).

The selected fiducial values of galaxy biases and the overall DESI sample descriptions are presented in Table 1. We use a limited galaxy samples: ELGs in the redshift range $z = 1.0\text{--}1.2$.

2.3. 21-cm auto-correlation

The auto power spectrum of 21-cm mapping in real space is written as,

$$\tilde{P}_{\delta_H \delta_H}(k) = P_{\delta_H \delta_H}(k) + P_{\epsilon_H \epsilon_H}, \quad (15)$$

where the stochastic noise $P_{\epsilon_H \epsilon_H}$ contains the shot noise, foreground noise and instrument noise denoted by $V_R \sigma_N^2$, N_{fore} and N_{inst} respectively. Here deterministic part $P_{\delta_H \delta_H}$ is given by

$$\begin{aligned} P_{\delta_H \delta_H}(k) &= b_{H1}^2 P_{\delta\delta}(k) + 2b_{H1}b_{H2}P_{b2,\delta}(k) \\ &+ 2b_{H1}b_{Hs2}P_{bs2,\delta}(k) \\ &+ 2b_{H1}b_{H3\text{nl}}\sigma_3^2(k)P_{\text{m}}^{\text{L}}(k) + b_{H2}^2 P_{b22}(k) \\ &+ 2b_{H2}b_{Hs2}P_{bs22}(k) + b_{Hs2}^2 P_{bs22}(k) \end{aligned} \quad (16)$$

with the bias b_{H1} defined as $\delta_H = b_{H1}\delta$.

The power spectrum of 21-cm density map and velocity is given by,

$$\tilde{P}_{\delta_H \Theta}(k) = P_{\delta_H \Theta}(k), \quad (17)$$

where $P_{\delta_H \Theta}(k)$ is given by,

$$\begin{aligned} P_{\delta_H \Theta}(k) &= b_{H1}P_{\delta\Theta}(k) + b_{H2}P_{b2,\Theta}(k) + b_{Hs2}P_{bs2,\Theta}(k) \\ &+ b_{H3\text{nl}}\sigma_3^2(k)P_{\text{m}}^{\text{L}}(k). \end{aligned} \quad (18)$$

Again, in the absence of velocity bias, the auto-power spectrum of HI velocity field is identical to $P_{\Theta\Theta}$. The higher-order polynomials $A_{HH}(k, \mu)$, $B_{HH}(k, \mu)$, $T_{HH}(k, \mu)$, and $F_{HH}(k, \mu)$ for 21-cm map can be expressed along the line of galaxy-galaxy auto-correlation Eqs. (11-14) in Section 2.2, with the replacement of bias b_{g1} with b_{H1} , and with the consideration of p_S for unit consistency. The general expression can be found from Eqs. (B10-B16) in Appendix B.

We consider the instrument thermal noise as a Gaussian random field given by,

$$\sigma_{\text{noise}} = T_{\text{sys}} \sqrt{\frac{4\pi f_{\text{sky}}}{\Omega_{\text{beam}} N_{\text{dish}} t_{\text{obs}} \Delta\nu}}, \quad (19)$$

Here T_{sys} is the total system temperature, which is the sum of the sky temperature and the receiver noise; $\Omega_{\text{beam}} \approx 1.133\theta_{\text{FWHM}}^2$ is the solid angle of the telescope main beam; f_{sky} is the fraction of sky covered by the survey, which e.g. for a box with the perpendicular size of $1000 \times 1000 \text{ Mpc}^2 h^{-2}$ at $z = 1.03$ is approximately $24 \times 24 \text{ deg}^2$ and therefore $f_{\text{sky}} \approx 0.014$; N_{dish} is the number of dishes in the array; t_{obs} is the integration time and $\Delta\nu$ is the bandwidth of each frequency channel. In our paper, we set $T_{\text{sys}} = 10\text{K}$ with $\Delta\nu = 1\text{MHz}$ and assign a total observation time $t_{\text{obs}} = 200\text{hrs}$. We consider $N_{\text{dish}} = 133$ according to the future MID telescope of the Square Kilometre Array (SKA) Observatory. As a result, the map could be with instrument noise at level $\sigma_{\text{noise}} = 0.01\text{mK}$ (in other cases: $f_{\text{sky}} t_{\text{obs}} = 200\text{hr}$, $\sigma_{\text{noise}} = 0.1\text{mK}$; $f_{\text{sky}} t_{\text{obs}} = 40\text{hr}$, $\sigma_{\text{noise}} = 0.22\text{mK}$).

Table 1. DESI survey specification

z	n_g^{LRG}	n_g^{ELG}	V	b_1^{LRG}	b_1^{ELG}	b_2^{LRG}	b_2^{ELG}
0.4–0.6	4.9×10^{-4}	1.6×10^{-4}	3.5	2.22	1.10	0.10	0.10
0.6–0.8	9.9×10^{-4}	1.4×10^{-3}	5.4	2.45	1.21	0.67	0.67
0.8–1.0	3.9×10^{-4}	1.7×10^{-3}	7.0	2.69	1.33	1.40	1.40
1.0–1.2	2.4×10^{-5}	9.8×10^{-4}	8.4	2.94	1.45	2.48	2.48
1.2–1.4	—	5.8×10^{-4}	9.4	—	1.57	—	3.91
1.4–1.6	—	2.3×10^{-4}	10.	—	1.70	—	5.68

NOTE—The expected number density of LRGs and ELGs are n_g^{LRG} ($h^3 \text{Mpc}^{-3}$) and n_g^{ELG} ($h^3 \text{Mpc}^{-3}$), respectively. V ($h^{-3} \text{Gpc}^3$) is the survey volume (comoving) at each redshift bin. For this study, we use ELG galaxies from a single redshift bin $z = 1.0\text{--}1.2$. These specific values are taken from the blueprints of the DESI experiment (DESI Collaboration et al. 2016). Fiducial values of bias for LRG and ELG are presented as well, calculated by the formulas $b_1^{\text{LRG}}(z)D(z) = 1.7$ and $b_1^{\text{ELG}}(z)D(z) = 0.84$ (DESI Collaboration et al. 2016), with D being the linear growth factor normalized to unity at present time, i.e., $D(z) = G_\delta(z)/G_\delta(0)$. For b_2^{LRG} and b_2^{ELG} , we use the “halofit” results (Takahashi et al. 2012). The ΛCDM model with Planck-estimated (Planck Collaboration et al. 2016) parameters is adopted as the fiducial cosmology.

The contribution from the intrinsic foreground power spectrum, denoted as N_{fore} , is roughly approximated as

$$N_{\text{fore}} = V_R(\bar{T}_{\text{sky}}f_r)^2, \quad (20)$$

where $\bar{T}_{\text{sky}} = 10\text{K}$ (Seo et al. 2010) and we assume unsuccessful removal of the foreground such that some of the intrinsic foreground power spectrum is left, e.g. with $f_r = 0.1$. This is to incorporate the reality that all wave modes are dominated by the foreground such as the Milky Way synchrotron, and a successful removal of the foreground is very difficult in some wave modes (see e.g. the so-called “avoidance scheme” to discard the small-wavenumber modes (Liu et al. 2014), caused by the difficulty of revealing the cosmic 21-cm background in the presence of the strong foreground). Even though the foreground has its own intrinsic power spectrum, we simply adopt the noise-like form (Eq. 20) to mimic the property that the foreground power spectrum does not correlate with the noise term in the galaxy survey. Because small wavenumber modes in the cosmic 21-cm signal can be removed in the foreground removal process due to over-fitting the line-of-sight wave modes, it might be useful to let a good amount of foreground reside. Our goal is then to see how cross correlation can enhance the cosmological parameter estimation in such situations. In this paper, we vary f_r to quantify the degree of foreground removal. Note that the minimum uncertainty in 21-cm auto-power spectrum, even in the ideal case

with perfect foreground removal, would be from the unavoidable shot noise power $P_{\epsilon_H \epsilon_H} \sim 100 h^{-3} \text{Mpc}^3$ (Section 2.1; Eq. 15) and the instrument noise.

2.4. Galaxy–21-cm cross-correlation

The cross-power spectrum in real space between galaxy and 21-cm map, which are tracers of dark matter density field, is expressed as (McDonald & Roy 2009; Saito et al. 2014)

$$\tilde{P}_{\delta_g \delta_H}(k) = P_{\delta_g \delta_H}(k), \quad (21)$$

where the stochastic noises disappear due to distinct characteristics of uncertainties. The term, $P_{\delta_g \delta_H}$, is only surviving part, and is given by,

$$\begin{aligned} P_{\delta_g \delta_H}(k) &= b_{g1}b_{H1}P_{\delta\delta}(k) \\ &+ b_{g1}b_{H2}P_{b2,\delta}(k) + b_{H1}b_{g2}P_{b2,\delta}(k) \\ &+ b_{g1}b_{Hs2}P_{bs2,\delta}(k) + b_{H1}b_{gs2}P_{bs2,\delta}(k) \\ &+ b_{g1}b_{H3\text{nl}}\sigma_3^2(k)P_{\text{m}}^{\text{L}}(k) + b_{H1}b_{g3\text{nl}}\sigma_3^2(k)P_{\text{m}}^{\text{L}}(k) \\ &+ b_{g2}b_{Hs2}P_{bs2}(k) + b_{H2}b_{gs2}P_{bs2}(k) \\ &+ b_{g2}b_{H2}P_{b22}(k) + b_{gs2}b_{Hs2}P_{b22}(k). \end{aligned} \quad (22)$$

To calculate the cross-power spectrum in redshift space $P_{gH}(k, \mu)$, the power spectrum of 21-cm map and velocity in real space $P_{\delta_H \Theta}(k)$ and the one of galaxy and velocity in real space $P_{\delta_g \Theta}(k)$ are needed as well. The power spectrum of 21-cm map and velocity for $P_{gH}(k, \mu)$

is given by,

$$\tilde{P}_{\delta_H \Theta}(k) = P_{\delta_H \Theta}(k), \quad (23)$$

where $P_{\delta_H \Theta}(k)$ is given by,

$$\begin{aligned} P_{\delta_H \Theta}(k) &= b_{H1} P_{\delta \Theta}(k) + b_{H2} P_{b2, \Theta}(k) + b_{Hs2} P_{bs2, \Theta}(k) \\ &+ b_{H3\text{nl}} \sigma_3^2(k) P_m^L(k), \end{aligned} \quad (24)$$

and the power spectrum of galaxy and velocity for $P_{gH}(k, \mu)$ is given by,

$$\tilde{P}_{\delta_g \Theta}(k) = P_{\delta_g \Theta}(k), \quad (25)$$

where $P_{\delta_g \Theta}(k)$ is given by,

$$\begin{aligned} P_{\delta_g \Theta}(k) &= b_{g1} P_{\delta \Theta}(k) + b_{g2} P_{b2, \Theta}(k) + b_{gs2} P_{bs2, \Theta}(k) \\ &+ b_{g3\text{nl}} \sigma_3^2(k) P_m^L(k), \end{aligned} \quad (26)$$

and the auto-power spectrum of velocity field in $P_{gH}(k, \mu)$ is identical to $P_{\Theta \Theta}$ in the absence of velocity bias.

The higher order polynomials for cross correlation $A_{gH}(k, \mu)$, $B_{gH}(k, \mu)$, $T_{gH}(k, \mu)$, and $F_{gH}(k, \mu)$ are described as follows:

$$\begin{aligned} A_{gH}(k, \mu) &= \sum_{n=1}^4 \mathcal{A}_{n, gH} \\ &= (G_\delta / \bar{G}_\delta)^2 (G_\Theta / \bar{G}_\Theta) \bar{\mathcal{A}}_{1, gH} + (G_\delta / \bar{G}_\delta) (G_\Theta / \bar{G}_\Theta)^2 \bar{\mathcal{A}}_{2, gH} \\ &+ (G_\delta / \bar{G}_\delta) (G_\Theta / \bar{G}_\Theta)^2 \bar{\mathcal{A}}_{3, gH} + (G_\Theta / \bar{G}_\Theta)^3 \bar{\mathcal{A}}_{4, gH}, \end{aligned} \quad (27)$$

$$\begin{aligned} B_{gH}(k, \mu) &= \sum_{n=1}^3 \mathcal{B}_{n, gH} \\ &= (G_\delta / \bar{G}_\delta)^2 (G_\Theta / \bar{G}_\Theta)^2 \bar{\mathcal{B}}_{1, gH} + (G_\delta / \bar{G}_\delta) (G_\Theta / \bar{G}_\Theta)^3 \bar{\mathcal{B}}_{2, gH} \\ &+ (G_\Theta / \bar{G}_\Theta)^4 \bar{\mathcal{B}}_{3, gH}, \end{aligned} \quad (28)$$

$$T_{gH}(k, \mu) = \sum_{n=1}^7 \mathcal{T}_{n, gH}$$

$$\begin{aligned} &= (G_\delta / \bar{G}_\delta)^2 (G_\Theta / \bar{G}_\Theta)^2 \bar{\mathcal{T}}_{1, gH} + (G_\delta / \bar{G}_\delta) (G_\Theta / \bar{G}_\Theta)^3 \bar{\mathcal{T}}_{2, gH} \\ &+ (G_\delta / \bar{G}_\delta) (G_\Theta / \bar{G}_\Theta)^3 \bar{\mathcal{T}}_{3, gH} + (G_\Theta / \bar{G}_\Theta)^4 \bar{\mathcal{T}}_{4, gH} \\ &+ (G_\delta / \bar{G}_\delta)^2 (G_\Theta / \bar{G}_\Theta)^2 \bar{\mathcal{T}}_{5, gH} + (G_\delta / \bar{G}_\delta) (G_\Theta / \bar{G}_\Theta)^3 \bar{\mathcal{T}}_{6, gH} \\ &+ (G_\Theta / \bar{G}_\Theta)^4 \bar{\mathcal{T}}_{7, gH}, \end{aligned} \quad (29)$$

and,

$$\begin{aligned} F_{gH}(k, \mu) &= \sum_{n=1}^3 \mathcal{F}_{n, gH} \\ &= (G_\delta / \bar{G}_\delta)^2 (G_\Theta / \bar{G}_\Theta)^2 \bar{\mathcal{F}}_{1, gH} + (G_\delta / \bar{G}_\delta) (G_\Theta / \bar{G}_\Theta)^3 \bar{\mathcal{F}}_{2, gH} \\ &+ (G_\Theta / \bar{G}_\Theta)^4 \bar{\mathcal{F}}_{3, gH}. \end{aligned} \quad (30)$$

Note that the exact expressions of $\bar{\mathcal{A}}_{n, gH}$, $\bar{\mathcal{B}}_{n, gH}$, $\bar{\mathcal{T}}_{n, gH}$, and $\bar{\mathcal{F}}_{n, gH}$ are included in Appendix B and that even higher-order contributions are consistently removed from all polynomial terms.

2.5. Fisher analysis

On large scales of our interest, the density and velocity fields are basically the small perturbations to the homogeneous background. When the higher-order contributions are small, the power spectrum is well described by the perturbed theoretical model. Then growth functions of density are accurately separate from the leading order of galaxy bias. In this work, non-linear description of power spectrum is adopted to break degeneracy between both contributions.

We are interested in analyzing galaxy survey and 21-cm mapping from the same sky, which makes the significant degeneracy among observables, $P_{gg}(k, \mu)$, $P_{gH}(k, \mu)$ and $P_{HH}(k, \mu)$. The full covariance matrix for cross-correlation statistics is given by (White et al. 2008),

$$C_{\tilde{P}_i \tilde{P}_j} = \frac{1}{N_P} \begin{pmatrix} 2P_{gg}^2 N_g^2 & 2P_{gg} P_{gH} N_g & 2P_{gH}^2 \\ 2P_{gg} P_{gH} N_g P_{gH}^2 + P_{gg} P_{HH} N_g N_H & 2P_{gH} P_{HH} N_H & 2P_{gH}^2 N_H^2 \\ 2P_{gH}^2 & 2P_{gH} P_{HH} N_H & 2P_{HH}^2 N_H^2 \end{pmatrix} \quad (31)$$

where i and j denote gg , gH and HH pairs, and N_g and N_H are given by

$$N_g = \left(1 + \frac{1}{\bar{n}_g P_{gg}} \right) \quad (32)$$

$$N_H = \left(1 + \frac{1}{\bar{n}_H P_{HH} / p_S^2} \right) \quad (33)$$

here the noise \bar{n} contains the shot, instrument and foreground noises. The weight of N_P in Eq. (31) is given by,

$$N_P = \frac{V_{\text{survey}}}{2(2\pi)^2} k^2 \Delta k \Delta \mu. \quad (34)$$

The Fisher matrix is evaluated with

$$F_{\alpha\beta} = \sum_{k,\mu} \sum_{i,j} \frac{\partial P_i(k,\mu)}{\partial \alpha} \left[C_{\tilde{P}_i \tilde{P}_j} \right]^{-1} \frac{\partial P_j(k,\mu)}{\partial \beta}. \quad (35)$$

The full result is presented in the following section with three different cases: (1) galaxy auto-correlation, (2) HI auto-correlation, (3) the joint analysis of the galaxy auto-correlation, HI auto-correlation and galaxy-HI cross-correlation.

3. CONSTRAINTS ON COSMOLOGICAL PARAMETERS

3.1. Precise simultaneous probe of σ_8 and $f\sigma_8$

The large-scale power spectrum in redshift space of our interest is being precisely probed through non-linear scale. The growth function of density fields parameterized by σ_8 and the leading order of coherent galaxy bias b_1 are slightly separable by non-linear smoothing effect around BAO scales up to the quasi-linear threshold limit. The density fluctuations of dark matter on crossing this threshold limit are significantly influenced by non-linear coupling, and leave distinct non-Gaussian signatures from the non-linear effects of galaxy bias. This non-linear evolution of density fluctuation in redshift space is determined by density and velocity growth parameters. Those are distinguishable effects of density and bias parameters, which are explained by local and non-local bias parameters in the previous section. In principle, b_1 and σ_8 are separately measurable using RSD effect by this distinct non-linear evolution of particle density perturbation and galaxy bias.

However there is still concern that the high degeneracy between coherent galaxy bias and σ_8 causes the poorer constraints on all other cosmological parameters up to the mild non-linear scales. While it can be resolved by extending k_{max} higher than $0.2 h \text{Mpc}^{-1}$, it will be interesting to observe the effect of full σ_8 marginalization on structure formation parameter $f\sigma_8$ through the combination of multiple probes between the galaxy survey and the 21-cm mapping. In the left panel of Figure 1, the toy model of that cross correlation is presented with varying $N_{\text{fore}} = (10^2, 10^3, 10^4) h^{-3} \text{Mpc}^3$. For example, the existing study using MeerKAT reports $N_{\text{fore}} \gtrsim 3000 h^{-3} \text{Mpc}^3$ at $k \sim 0.1 h \text{Mpc}^{-1}$ with $N_{\text{fg}} = 4$ (Figure 4 of Cunningham et al. 2022; N_{fg} is the num-

ber of principal components fitting out the radio foreground⁴) with the reported sky coverage of $\sim 200 \text{ deg}^2$. The galaxy auto-power spectra $P_{gg}(k, \mu)$ with the coherent bias $b_{g1} = 1.5$ are presented by black dotted curves by varying $\mu = (0.05, 0.45, 0.85)$ from bottom to top. The 21-cm auto-power spectra $P_{HH}(k, \mu)$ with the coherent bias $b_{H1} = 1.1$ are presented as red dashed curves with various foreground noises which cover all ranges of foreground noise from optimistic to conservative predictions. The cross spectra $P_{gH}(k, \mu)$ are shown as black dot-dashed curves.

Next, we present constraint on σ_8 in the right panel of Figure 1. As it is measurable through higher order terms in perturbative computation, the constraint becomes poorer than other parameters which are probed all contributions including leading order. But we find that we are able to probe σ_8 around several percentage precision. It indicates that we can access to both density and velocity information with one-single experiment of spectroscopy scanning of sky. Both the leading and next order galaxy local biases are independently varied as well as σ_8 , while non-local bias is fed by updated b_1 instead of full variation. Galaxy biases are poorly determined, but this error is not much propagated through cosmological constraints except for σ_8 .

In the right figure of Figure 1 shows the impact of this uncertainty in constraining the growth of structure. Here, the plotted result is the two-dimensional contour of the expected 1σ constraint, which is estimated at the specific redshift bin, $1.0 < z < 1.2$. The parameter σ_p is significantly correlated with the linear growth rate $f\sigma_8$, and the analysis using the power spectrum alone, depicted as dotted contour, exhibits a strong parameter degeneracy. This is partly due to the small cut-off wavenumber, $k_{\text{max}} = 0.2 h \text{Mpc}^{-1}$, below which the damping term, expressed as function of $(k\mu)^2$, is monotonically varied along the direction μ , and the behavior looks very similar when we vary f . Interestingly, however, the direction of the parameter degeneracy differs from that of the power spectrum case.

The cosmological constraint between σ_8 and $f\sigma_8$ is presented in four panels of right figure in Figure 1, with variation of foreground noise. As it is described above, both σ_8 and $f\sigma_8$ are fully marginalized by its own systematical uncertainties represented by σ_p and b_1 respectively. The density fluctuation σ_8 is not well constrained

⁴ While Cunningham et al. (2022) extends N_{fg} up to 30, even at $N_{\text{fg}} = 10$ the loss of the power spectrum is significant at $k \sim 0.1 h \text{Mpc}^{-1}$. Our goal is to preserve the large-scale power as much as possible for cross-correlation, and thus $N_{\text{fg}} = 4$ case roughly gives a practical estimation of the foreground contamination.

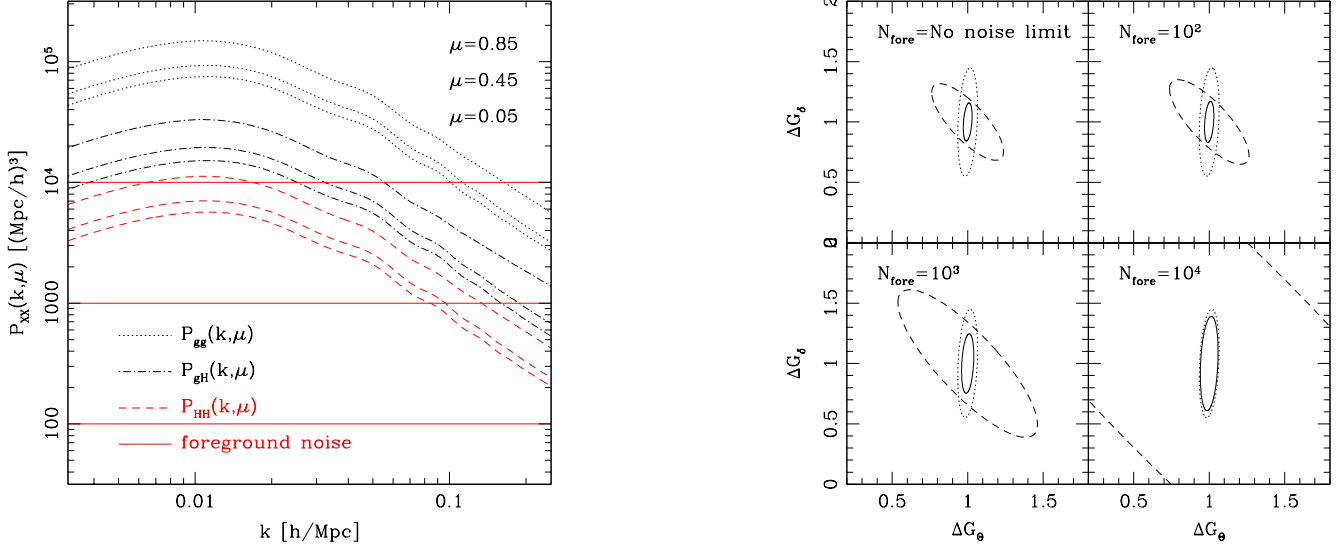


Figure 1. *Left:* The toy model power spectra of P_{gg} , P_{gH} and P_{HH} represented by dotted, dot-dash and dashed curves respectively are presented with varying $N_{\text{fore}} = (10^2, 10^3, 10^4)(h^{-1} \text{Mpc})^3$ presented by solid lines from bottom to top. The anisotropic power spectra are presented by varying $\mu = (0.05, 0.45, 0.85)$ from bottom to top. *Right:* The contour plots between G_δ and G_Θ are presented with galaxy auto spectrum case, HI auto spectrum case and full cross spectra case presented by dotted, dashed, and solid contours. The given foreground noise level along with no foreground noise limit is denoted in each panel.

beyond 10% with galaxy–galaxy auto–correlation alone, which is caused by high degeneracy between σ_8 and b_1 . The similar constraint on σ_8 is observed with HI–HI auto–correlation case with which the precision level is highly dependent on the quality of foreground noise cleaning procedure. Only when the signal is clearly visible through all non–linear scales, the cosmological constraint on σ_8 becomes closer to galaxy–galaxy auto–correlation case.

However, the cosmological constraint of σ_8 is significantly improved with cross–correlation statistics, which is presented by solid contours in the right figure of Figure 1. The level of precision of σ_8 constraint exhibits less than 5%, which can be considered as a precise probe of the density fluctuation. In addition, the velocity growth function $f\sigma_8$ constraint is estimated under 1% precision level. Note that this high precision estimation is relatively free from the uncertainty of foreground noise cleaning procedure.

3.2. Benefit for distance measurements

A precision measurement of the BAO scale is the key to determining the geometric distances, $D_A(z)$ and $H^{-1}(z)$, through the A-P effect. Although the acoustic structure imprinted on the power spectrum actually depends on cosmology, the counterpart of the acoustic oscillations is precisely observed in the CMB anisotropies, and with the cosmological results by WMAP and Planck

as prior information, the BAO can be used as standard ruler. At $k \lesssim 0.2 h \text{Mpc}^{-1}$, the galaxy power spectrum is supposed to be described by the leading-order perturbation, where the acoustic signature is clearly visible. In the presence of galaxy bias, the only uncertainty is the clustering amplitude, however, this does not seriously affect the measurement of the characteristic scales of BAO.

In Figure 2, the forecast result for the statistical errors of the angular diameter distance D_A is shown in the x–axis. With the DESI-like survey, constraints on D_A from the power spectrum (dotted contours) becomes comparable to 21 cm ideal experiment (dashed contours), although the constraining power of the 21-cm experiment becomes rapidly worsen as increasing the foreground noise. Note that if all the other parameters such as growth rate $f\sigma_8$ and galaxy bias are known a priori, D_A can be measured with sub–percentage accuracy. However, the growth rate and the linear bias are mostly degenerate with D_A , particularly in the limit of $\mu \rightarrow 0$. Combining both the galaxy and the 21-cm experiments, depicted as solid contour, the constraint on D_A will not be much improved.

Note that a comparable result of the constrained values is understood from the signal–to–noise. The signal–to–noise for 21 cm experiment is higher than that of the power spectrum with the no noise limit. Accordingly, the cosmological constraints on distances from 21

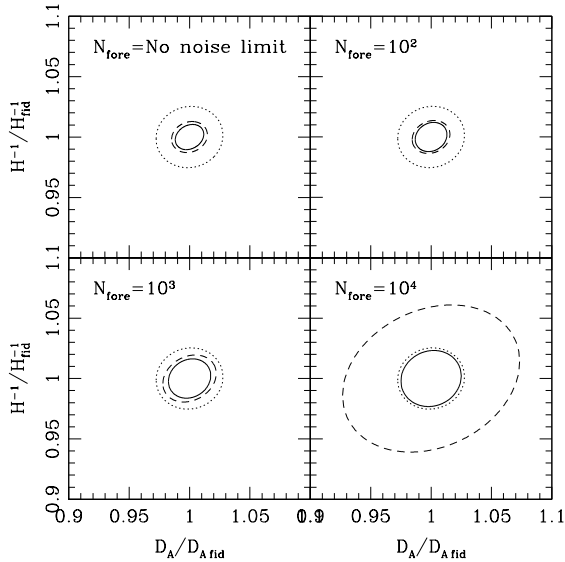


Figure 2. The contour plots between $D_A/D_{A,\text{fid}}$ and $H^{-1}/H_{\text{fid}}^{-1}$ are presented with galaxy auto spectrum case, HI auto spectrum case and full cross spectra case presented by dotted, dashed, and solid contours. The given foreground noise level is denoted in each panel.

cm experiment become better than those from power spectrum of galaxy survey, as shown in Figure 2. Thus, combining both galaxy survey and 21 cm experiment provides no opportunity to improve the constraints on D_A . This result is consistent with the forecast using angular cross-correlation power spectra in Shi et al. (2020) in the sense that our constraining power is around 2~3 per cent for $N_{\text{fore}} \simeq 10^4 h^{-3} \text{ Mpc}^3$ and it increases slower as the quality of foreground removal gets better than the one for HI auto-correlation case. Note that our prediction is based on the combination of the auto-correlations of HI and galaxy as well as the cross-correlation between galaxy and HI while Shi et al. (2020) only utilizes cross-correlation and 2.7 per cent is the mean result averaged from the 10 redshift bins. On the other hand, the determination of radial distance H^{-1} is more difficult than that of D_A . The angular coordinate dependence of the error on H^{-1} is presented in the left panel of Figure 1. The information on H^{-1} is most imprinted at the limit of $\mu \rightarrow 1$, at which the observed spectrum is influenced by RSD, mainly due to the non-linear smearing effect. Because of this, the resultant statistical precision is poorer than that of D_A by a factor 2. In comparison of the solid and the dot-dashed curves, the off-diagonal elements of the covariance matrix do not significantly reduce the constraining power.

Table 2. Error forecast on x_{HI}

N_{fore}	galaxy-galaxy	21-cm-21-cm	galaxy-21-cm
no noise	—	13%	0.32%
$10^2 h^{-1} \text{ Mpc}^3$	—	15%	0.34%
$10^3 h^{-1} \text{ Mpc}^3$	—	28%	0.57%
$10^4 h^{-1} \text{ Mpc}^3$	—	140%	2.6%

NOTE—The fractional errors $\sigma(x_{\text{HI}})/x_{\text{HI}}$ are presented with varying toy model foreground noises (N_{fore}).

3.3. Astrophysical implication: neutral hydrogen fraction

Our result shows that the joint analysis on power spectra (gg, gH and HH) can very strongly constrain x_{HI} , as is shown in Table 2. Percent level or even the sub-percent level we expect in x_{HI} estimation far surpasses the currently available estimations giving $\sigma(x_{\text{HI}})/x_{\text{HI}} \sim 1$. Depending on the degree of the systematic uncertainties (N_{fore} , not restricted to the sky brightness but also inclusive of the antenna systematics and shot noises due to the finite number of galaxies and 21-cm sources), the 21-cm auto-correlation is found to constrain x_{HI} to a few tens of per cent when $N_{\text{fore}} \lesssim 10^3 h^{-3} \text{ Mpc}^3$. However, the joint analysis (cross+auto) is found to constrain x_{HI} to sub-percent levels when $N_{\text{fore}} \lesssim 10^3 h^{-3} \text{ Mpc}^3$, and to a few-percent level even when $N_{\text{fore}} \simeq 10^4 h^{-3} \text{ Mpc}^3$. We show our sanity check on the smallness of our estimated $\sigma(x_{\text{HI}})$ in Appendix C. This is a very useful result because x_{HI} encapsulates the post-reionization astrophysics as a whole which is still poorly constrained.

We believe that such a high accuracy in x_{HI} estimation is thanks to the capability to break the degeneracy between b_{HI} (more accurately, the leading order bias b_{H1}) and x_{HI} . We demonstrate this by examining the dependence of the anisotropic power spectra on b_{HI} and μ . As seen in Figure 3, while the impact of x_{HI} on power spectra are trivial (working as a simple multiplier to power spectra), the impact of b_{HI} is significant. Dependence of the power spectra on b_{HI} gets amplified as μ becomes larger. Therefore, according to our nonlinear formalism, observing the anisotropic power spectra can constrain b_{HI} . This then breaks the usual degeneracy between b_{HI} and x_{HI} that has been reported on previous studies (e.g. Cunningham et al. 2022).

Such a tight constraint on x_{HI} could be one of the most accurate, and can help us understand how post-reionization physics has proceeded. So far, constraints come mainly from observing the Lyman- α for-

est (Rao et al. 2006; Grasha et al. 2020) with values ranging from $\Omega_{\text{HI}}(z) \equiv x_{\text{HI}}(z)\Omega_{\text{H,0}} = (0.7 \pm 0.3) \times 10^{-3}$ (Rao et al. 2006) to $\Omega_{\text{HI}}(z) = (1.2 \pm 0.3) \times 10^{-3}$ (Grasha et al. 2020) at $z \simeq 1$. Direct detection of 21-cm emission objects can only give lower limits to x_{HI} at the moment due to the limited sensitivity of telescopes compared to the smallness of their usual flux (Jones et al. 2018; Chowdhury et al. 2020; Zhang et al. 2024). In other words, currently $\sigma(x_{\text{HI}})/x_{\text{HI}} \simeq 1$ and we expect the measure of $P_{g\text{H}}$ for the joint analysis with P_{gg} and P_{HH} can improve the constraint to a very ideal level.

One could in principle further constrain the physics of the hydrogen clumps with such a tight constraint on x_{HI} . Suppose that we could model the hydrogen clump distribution with a simple hydrogen mass function dn/dM_{HI} (comoving clump number density per unit hydrogen clump mass), possibly in a form such as the Schechter function, and assume the rest of the universe fully ionized, then we will have

$$x_{\text{HI}} = \frac{1}{\Omega_{\text{H,0}}\rho_{\text{crit},0}} \int_{M_{\text{HI,Min}}} M_{\text{HI}} \frac{dn}{dM_{\text{HI}}} dM_{\text{HI}}, \quad (36)$$

where $M_{\text{HI,Min}}$ is the minimum hydrogen clump mass. Therefore, once the mass function is modelled to a certain accuracy and extrapolated to the small-mass end that may not be detected as individual galaxies both in the galaxy survey and the 21-cm survey, we may be able to further constrain the minimum hydrogen clump mass $M_{\text{HI,Min}}$. $M_{\text{HI,Min}}$ is expected to be determined primarily by the Jeans-mass filtering of the heated intergalactic medium by photo-heating, and thus this can be extended to the understanding of the post-reionization process.

4. RESULTS AND CONCLUSION

4.1. Simultaneous probe of σ_8 and $f\sigma_8$; contribution of non-linearity

It is presented that growth functions of density and velocity fields σ_8 and $f\sigma_8$ are precisely measured by cross correlation between galaxy survey and HI emission experiment. If dark matter particles are un-biasedly traceable, then both parameters will be probed by anisotropy feature alone. The density growth function σ_8 is probed at $\mu \rightarrow 0$ limit as a pivot parameter with the rotation of μ direction. With precise determination of the pivot point, $f\sigma_8$ can be measurable through squeezing effect with increasing μ in redshift distortion. In reality, dark particle fluctuation is indirectly probed by galaxy or emission tracers. The pivot location of σ_8 is vaguely seen with biased tracers caused by degeneracy

from galaxy bias. Thus σ_8 and $f\sigma_8$ is not measured simultaneously with auto correlation alone.

The leading order bias b_X is not separable from σ_8 up to linear scale of k . At crossing further into smaller scale of quasi-linear scale of k , galaxy bias b_X is mingled with density fluctuation σ_8 through higher order perturbations. The response of power spectrum with a variation of σ_8 becomes dependent the value of leading order galaxy bias parameter. If alternative power spectra from diverse galaxy probes are cross-correlated, this distinct response causes tilted orientation of covariance between σ_8 and b_X . When the pivot point σ_8 is probed by distinct non-linearity through cross-correlation, $f\sigma_8$ is precisely determined.

The ELG galaxy bias b_g with relatively high mass galaxy around $10^{12}M$ is expected around 1.4, and HI emission is observed by much smaller galaxies around $10^{10}M$ with the assumed galaxy bias $b_{\text{HI}} = 1.1$. As the mass profile of observed galaxies is strongly related to the leading order bias, this assumed galaxy biases are reasonable. The higher order perturbed terms are presented in this manuscript, and the variation of power spectra becomes different with galaxy bias through non-linearity. It is observed the tilted covariance between σ_8 and $f\sigma_8$ for each auto-correlations of galaxy survey and HI emission. This distinct correlation leads us to separate σ_8 and $f\sigma_8$.

4.2. Precise probe of x_{HI} ; contribution of anisotropy

The measured power spectrum is highly sensitive to the variation of overall amplitude, and the signal to noise has been improved with recent wide deep field experiment. If all other cosmological and nuisance parameters are pre-determined, then x_{HI} will be determined in the sub-percentage level. However, the constraint on a parameter with an featureless overall amplitude contribution becomes much poorer in marginalization with other parameters. For instance, x_{HI} parameter is most degenerate with galaxy bias b_{HI} .

The anisotropy caused squeezing effect in redshift space provides a unique opportunity to break degeneracy between x_{HI} and b_{HI} . While the peculiar velocity is immune from galaxy bias in galaxy survey, the temperature effect on HI emission is equally contributing on both density and velocity perturbation. Thus the featureless influence on power spectrum with variation of x_{HI} is maintained even in the limit of $\mu \rightarrow 1$, but the power spectrum change becomes minimal at the same limit. The degeneracy between x_{HI} and b_{HI} is broken by this anisotropy in redshift space distortion.

This degeneracy break explained in the above paragraph will not be observed with 21-cm auto power spec-

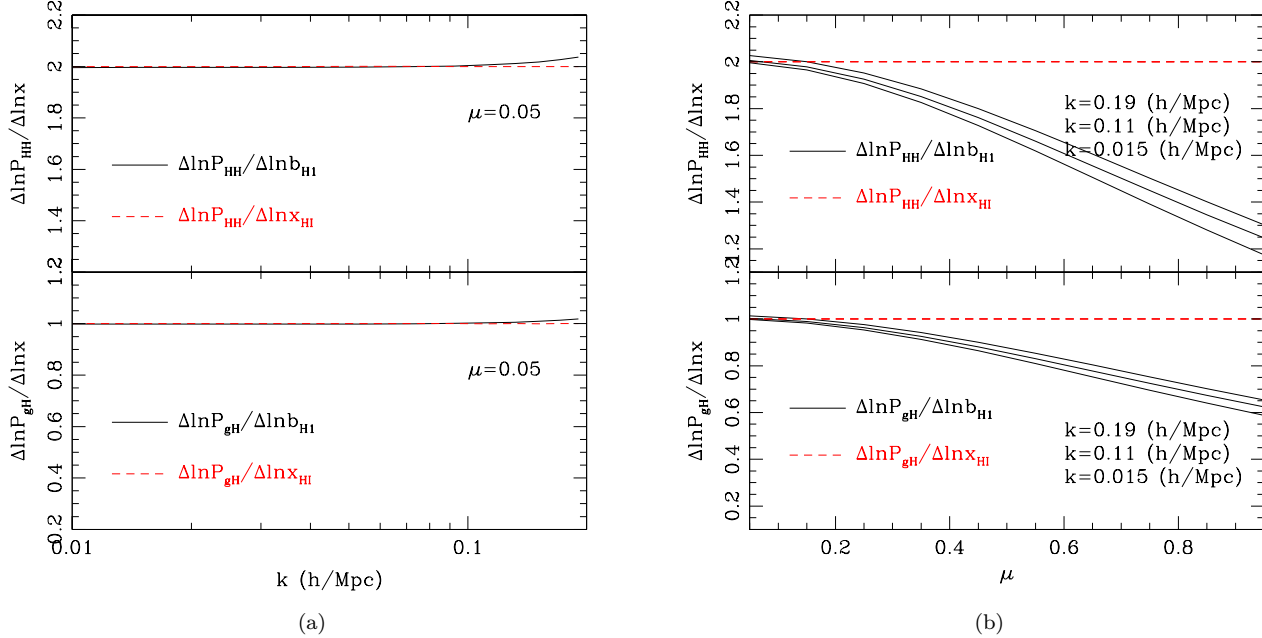


Figure 3. (a) Variations of power spectra of HI-HI (top) and g-HI (bottom) against the HI bias b_{HI} and the HI fraction x_{HI} in terms of k at $\mu = 0.05$. (b) Same as (a) but also with varying k (smallest to largest from top to bottom curves), now in terms of μ . Overall, dependence of the anisotropic power spectra on μ and b_{HI} makes it possible for our nonlinear prescription to break the degeneracy between b_{HI} and x_{HI} .

trum alone. There is an additional degeneracy between σ_8 and b_{HI} which is broken by the cross-correlation. Here is the chain of degeneracy break; 1) galaxy bias is separable from σ_8 by cross-correlation statistics through distinct non-linearity, 2) x_{HI} parameter becomes distinguished from galaxy bias through anisotropy in redshift distortion.

Accurate estimation of x_{HI} will of course enable us to probe its temporal evolution. We used a rather restricted range of redshift, $1.0 < z < 1.2$, in this study. However, we can extend the analysis to more finely-sampled redshift bins in a wider redshift domain to estimate the evolution of x_{HI} . Roughly put, $\sigma(x_{\text{HI}}) \propto \Delta r^{-0.5}$, where Δr is the longitudinal comoving distance in a given redshift bin, assuming a simple sample variance. Therefore, about a percent-level accuracy is warranted for $x_{\text{HI}}(z)$ measurement at e.g. ~ 20 redshift bins from $2 \gtrsim z \gtrsim 0$.

ACKNOWLEDGMENTS

We would like to thank Takahiro Nishimichi for useful discussions and comments. Numerical calculations were performed using a high performance computing cluster in the Korea Astronomy and Space Science Institute. KA is supported by the National Research Foundation of Korea (NRF) RS-2021-NR058956, RS-2025-16302968 and the Korea Astronomy and Space Science Institute under the R&D program (Project No. 2025-9-844-00) supervised by the Korea AeroSpace Administration. F.S acknowledges the support from the National SKA Program of China (2022SKA0110200 and 2022SKA0110202). YSS is supported by the National Research Foundation of Korea (NRF) grant funded by the Korea government (MIST) RS-2021-NR058702.

APPENDIX

A. DESCRIPTION OF HYBRID RSD MODEL FOR MATTER POWER SPECTRUM

The evolution of the density and peculiar velocity fields is traditionally parameterized by σ_8 and $f\sigma_8$. Both are related to the growth functions of G_δ and G_Θ written as below,

$$\sigma_8^2(z) = \frac{G_\delta^2(z)}{2\pi^2} \int W_8^2(k) k^2 P_{\delta\delta}^i(k) dk, \quad (\text{A1})$$

$$(f\sigma_8)^2(z) = \frac{G_\Theta^2(z)}{2\pi^2} \int W_8^2(k) k^2 P_{\delta\delta}^i(k) dk. \quad (\text{A2})$$

The window function W_8 is given by,

$$W_8 = \frac{3j_1(kR_8)}{kR_8}, \quad (\text{A3})$$

where j_1 is the first-order spherical Bessel function, and $R_8 = 8h^{-1}\text{Mpc}$. We intend to simultaneously probe σ_8 and $f\sigma_8$ by exploiting the G_δ and G_Θ parameters.

In the hybrid approach of modelling the RSD effect, the theoretical spectra $\bar{P}_{XY}^{\text{th}}(k, z)$ ($X, Y = \delta$ or Θ) are computed by the RegPT treatment (Taruya et al. 2012), in which all the statistical quantities including power spectrum are expanded in terms of the multi-point propagators up to the two-loop order as,

$$\begin{aligned} \bar{P}_{XY}(k, z) = & \bar{\Gamma}_X^{(1)}(k, z)\bar{\Gamma}_Y^{(1)}(k, z)\bar{P}^i(k) + 2 \int \frac{d^3\vec{q}}{(2\pi)^3} \bar{\Gamma}_X^{(2)}(\vec{q}, \vec{k} - \vec{q}, z)\bar{\Gamma}_Y^{(2)}(\vec{q}, \vec{k} - \vec{q}, z)\bar{P}^i(q)\bar{P}^i(|\vec{k} - \vec{q}|) \\ & + 6 \int \frac{d^3\vec{p}d^3\vec{q}}{(2\pi)^6} \bar{\Gamma}_X^{(3)}(\vec{p}, \vec{q}, \vec{k} - \vec{p} - \vec{q}, z)\bar{\Gamma}_Y^{(3)}(\vec{p}, \vec{q}, \vec{k} - \vec{p} - \vec{q}, z)\bar{P}^i(p)\bar{P}^i(q)\bar{P}^i(|\vec{k} - \vec{p} - \vec{q}|). \end{aligned} \quad (\text{A4})$$

Here \bar{P}^i is the initial power spectrum, and $\bar{\Gamma}_X^{(n)}$ is the $(n+1)$ -point propagator. The explicit expression of $\bar{\Gamma}_X^{(n)}$ can be found in Section 2.2 of Song et al. (2018).

While the prescription given above is supposed to give an accurate theoretical prediction at higher redshifts and larger scales, Song et al. (2018) reported that the RegPT prediction of \bar{P}_{XY} at a low redshift (to be precise $z = 0.5$) exhibits a small deviation from N -body simulations at $k > 0.1 h \text{Mpc}^{-1}$. Although this might be partly ascribed to the systematics in the N -body simulations, a lack of higher-order terms as well as a small systematics in the PT calculations is known to sensitively affect the high- k prediction. Here, we characterize the difference between the measured and predicted power spectra by $\bar{P}_{XY}^{\text{res}}$. We then divide the power spectrum into two pieces:

$$\bar{P}_{XY}(k, z) = \bar{P}_{XY}^{\text{th}}(k, z) + \bar{P}_{XY}^{\text{res}}(k, z), \quad (\text{A5})$$

where \bar{P}_{XY}^{th} represents the PT prediction with $\bar{\mathcal{O}}_{X,n}^{(m)} \rightarrow 0$. Collecting all the uncertainties introduced in the multi-point propagators, the residual power spectrum $\bar{P}_{XY}^{\text{res}}$ is schematically expressed as

$$\begin{aligned} \bar{P}_{XY}^{\text{res}} = & \bar{G}_X \bar{G}_Y \bar{G}_\delta^4 \left\{ \left[\bar{\mathcal{O}}_{Y,5}^{(1)} + \text{higher} \right] \bar{P}^i + \left[\bar{\mathcal{O}}_{X,5}^{(1)} + \text{higher} \right] \bar{P}^i \right. \\ & + \int \left[\bar{\mathcal{O}}_{Y,4}^{(2)} \bar{F}_Y^{(2)} + \text{higher} \right] \bar{P}^i \bar{P}^i + \int \left[\bar{\mathcal{O}}_{X,4}^{(2)} \bar{F}_X^{(2)} + \text{higher} \right] \bar{P}^i \bar{P}^i \\ & \left. + \int \int \left[\bar{\mathcal{O}}_{Y,3}^{(3)} \bar{F}_Y^{(3)} + \text{higher} \right] \bar{P}^i \bar{P}^i \bar{P}^i + \int \int \left[\bar{\mathcal{O}}_{X,3}^{(3)} \bar{F}_X^{(3)} + \text{higher} \right] \bar{P}^i \bar{P}^i \bar{P}^i \right\}. \end{aligned} \quad (\text{A6})$$

Here, the uncertainty $\bar{\mathcal{O}}_{X,n}^{(m)}$ is assumed to be small, and to be perturbatively treated. The expression implies that apart from a detailed scale-dependent behavior, time dependence is characterized by $G_X G_Y G_\delta^4$. Thus, once we calibrate the $\bar{P}_{XY}^{\text{res}}$ at a given redshift, we may use it for the prediction at another redshift by simply rescaling the calibrated residuals. Furthermore, for the cosmological models close to the fiducial model, the scale dependence of the higher-order PT corrections is generally insensitive to the cosmology, and we may also apply the calibrated $\bar{P}_{XY}^{\text{res}}$ to other cosmological models.

B. DESCRIPTION OF HIGHER-ORDER OF HYBRID RSD MODEL FOR AUTO AND CROSS POWER SPECTRUM FOR TWO TRACERS

Next we introduce the method to estimate the higher order terms of the clustering of the tracers by generalizing the expressions for the higher order terms of auto power spectrum of dark matter in Sec. 2.3 of Song et al. (2018) to

the ones of cross-power spectrum between tracer a and tracer b. They are incorporated into Eq. (6) to calculate the general cross-power spectrum including higher order terms. To begin with, let us consider the A term.

$$\begin{aligned} A_{ab}(k, \mu) &= j_1 \int d^3 \mathbf{x} e^{i\mathbf{k} \cdot \mathbf{x}} \langle A_1 A_2^a A_3^b \rangle_c \\ &= j_1 \int d^3 \mathbf{x} e^{i\mathbf{k} \cdot \mathbf{x}} \langle (u_z - u'_z)(b_{a1}\delta + \nabla_z u_z)(b_{b1}\delta' + \nabla_z u'_z) \rangle_c, \end{aligned} \quad (\text{B7})$$

where A_1, A_2^a and A_3^b are defined in Sec. 2.1. From the explicit form, the A term is split into four pieces. Here, we specifically write down the expressions in fiducial cosmological model:

$$\bar{A}_{ab}(k, \mu) = \sum_{n=1}^4 \bar{\mathcal{A}}_{n,ab}. \quad (\text{B8})$$

The barred quantities indicate those computed/measured in fiducial cosmological model and the explicit form of $\bar{\mathcal{A}}_n$ is given below:

$$\begin{aligned} \bar{\mathcal{A}}_{1,ab} &= 2j_1 \int d^3 \mathbf{x} e^{i\mathbf{k} \cdot \mathbf{x}} \langle u_z(\mathbf{r})\delta(\mathbf{r})\delta(\mathbf{r}') \rangle_c b_{a1}b_{b1}, \\ \bar{\mathcal{A}}_{2,ab} &= j_1 \int d^3 \mathbf{x} e^{i\mathbf{k} \cdot \mathbf{x}} \langle u_z(\mathbf{r})\delta(\mathbf{r})\nabla_z u_z(\mathbf{r}') \rangle_c (b_{a1} + b_{b1}), \\ \bar{\mathcal{A}}_{3,ab} &= j_1 \int d^3 \mathbf{x} e^{i\mathbf{k} \cdot \mathbf{x}} \langle u_z(\mathbf{r})\nabla_z u_z(\mathbf{r})\delta(\mathbf{r}') \rangle_c (b_{a1} + b_{b1}), \\ \bar{\mathcal{A}}_{4,ab} &= 2j_1 \int d^3 \mathbf{x} e^{i\mathbf{k} \cdot \mathbf{x}} \langle u_z(\mathbf{r})\nabla_z u_z(\mathbf{r})\nabla_z u_z(\mathbf{r}') \rangle_c, \end{aligned} \quad (\text{B9})$$

where the biases b_{a1} and b_{b1} are defined as $\delta_a = b_{a1}\delta$ and $\delta_b = b_{b1}\delta$ where the subscripts a and b stand for either g or H. These terms are measured from N -body simulations according to Zheng & Song (2016). To apply the measured results to the prediction in other cosmological models, we assume the scaling ansatz, as similarly adopted in the prediction of power spectrum P_{XY} . That is, assuming that the scale-dependence of each term is insensitive to the cosmology, the prediction of each term is made by simply rescaling the measured results. The proposition made here is that the time-dependence of each term is approximately determined by the leading-order growth factor dependence of u_z and δ . Then, A_{ab} term in general cosmological model is expressed as

$$\begin{aligned} A_{ab}(k, \mu) &= \sum_{n=1}^4 \mathcal{A}_{n,ab} = (G_\delta/\bar{G}_\delta)^2 (G_\Theta/\bar{G}_\Theta) \bar{\mathcal{A}}_{1,ab} \\ &\quad + (G_\delta/\bar{G}_\delta) (G_\Theta/\bar{G}_\Theta)^2 \bar{\mathcal{A}}_{2,ab} + (G_\delta/\bar{G}_\delta) (G_\Theta/\bar{G}_\Theta)^2 \bar{\mathcal{A}}_{3,ab} \\ &\quad + (G_\Theta/\bar{G}_\Theta)^3 \bar{\mathcal{A}}_{4,ab}. \end{aligned} \quad (\text{B10})$$

We then apply the same manner to other higher-order corrections. Starting from the explicit form of B ,

$$\begin{aligned} B_{ab}(k, \mu) &= j_1^2 \int d^3 \mathbf{x} e^{i\mathbf{k} \cdot \mathbf{x}} \langle A_1 A_2^a \rangle_c \langle A_1 A_3^b \rangle_c, \\ &= j_1^2 \int d^3 \mathbf{x} e^{i\mathbf{k} \cdot \mathbf{x}} \langle (u_z - u'_z)(b_{a1}\delta + \nabla_z u_z) \rangle_c \langle (u_z - u'_z)(b_{b1}\delta' + \nabla_z u'_z) \rangle_c, \end{aligned}$$

we divide this correction in fiducial cosmology into several pieces, and the scaling ansatz leads to the following predictions:

$$\bar{B}_{ab}(k, \mu) = \sum_{n=1}^3 \bar{\mathcal{B}}_{n,ab},$$

where the explicit forms of $\bar{\mathcal{B}}_{n,ab}$ are given below

$$\bar{\mathcal{B}}_{1,ab} = -j_1^2 \int d^3 \mathbf{x} e^{i\mathbf{k} \cdot \mathbf{x}} \langle u_z(\mathbf{r}')\delta(\mathbf{r}) \rangle_c \langle u_z(\mathbf{r})\delta(\mathbf{r}') \rangle_c b_{a1}b_{b1},$$

$$\begin{aligned}\bar{\mathcal{B}}_{2,ab} &= -j_1^2 \int d^3\mathbf{x} e^{i\mathbf{k}\cdot\mathbf{x}} \langle u_z(\mathbf{r}') \delta(\mathbf{r}) \rangle_c \langle u_z(\mathbf{r}) \nabla_z u_z(\mathbf{r}') \rangle_c (b_{a1} + b_{b1}), \\ \bar{\mathcal{B}}_{3,ab} &= -j_1^2 \int d^3\mathbf{x} e^{i\mathbf{k}\cdot\mathbf{x}} \langle u_z(\mathbf{r}') \nabla_z u_z(\mathbf{r}) \rangle_c \langle u_z(\mathbf{r}) \nabla_z u_z(\mathbf{r}') \rangle_c.\end{aligned}\quad (\text{B11})$$

Thus, B_{ab} term in general cosmological model is expressed as

$$\begin{aligned}B_{ab}(k, \mu) &= \sum_{n=1}^3 \mathcal{B}_{n,ab} = (G_\delta/\bar{G}_\delta)^2 (G_\Theta/\bar{G}_\Theta)^2 \bar{\mathcal{B}}_{1,ab} \\ &\quad + (G_\delta/\bar{G}_\delta) (G_\Theta/\bar{G}_\Theta)^3 \bar{\mathcal{B}}_{2,ab} + (G_\Theta/\bar{G}_\Theta)^4 \bar{\mathcal{B}}_{3,ab}.\end{aligned}\quad (\text{B12})$$

The explicit expression for $T_{ab}(k, \mu)$ is

$$\begin{aligned}T_{ab}(k, \mu) &= \frac{1}{2} j_1^2 \int d^3\mathbf{x} e^{i\mathbf{k}\cdot\mathbf{x}} \langle A_1^2 A_2^a A_3^b \rangle_c \\ &= \frac{1}{2} j_1^2 \int d^3\mathbf{x} e^{i\mathbf{k}\cdot\mathbf{x}} \langle (u_z - u'_z)^2 (b_{a1}\delta + \nabla_z u_z)(b_{b1}\delta' + \nabla_z u'_z) \rangle_c.\end{aligned}$$

This equation can be divided as well into seven pieces in fiducial cosmology:

$$\bar{T}_{ab}(k, \mu) = \sum_{n=1}^7 \bar{\mathcal{T}}_{n,ab},$$

where the explicit forms of $\bar{\mathcal{T}}_{n,ab}$ are given below:

$$\begin{aligned}\bar{\mathcal{T}}_{1,ab} &= j_1^2 \int d^3\mathbf{x} e^{i\mathbf{k}\cdot\mathbf{x}} \langle u_z(\mathbf{r}) u_z(\mathbf{r}) \delta(\mathbf{r}) \delta(\mathbf{r}') \rangle_c b_{a1} b_{b1}, \\ \bar{\mathcal{T}}_{2,ab} &= j_1^2 \int d^3\mathbf{x} e^{i\mathbf{k}\cdot\mathbf{x}} \langle u_z(\mathbf{r}) u_z(\mathbf{r}) \delta(\mathbf{r}) \nabla_z u_z(\mathbf{r}') \rangle_c (b_{a1} + b_{b1}), \\ \bar{\mathcal{T}}_{3,ab} &= j_1^2 \int d^3\mathbf{x} e^{i\mathbf{k}\cdot\mathbf{x}} \langle u_z(\mathbf{r}) u_z(\mathbf{r}) \nabla_z u_z(\mathbf{r}) \delta(\mathbf{r}') \rangle_c (b_{a1} + b_{b1}), \\ \bar{\mathcal{T}}_{4,ab} &= j_1^2 \int d^3\mathbf{x} e^{i\mathbf{k}\cdot\mathbf{x}} \langle u_z(\mathbf{r}) u_z(\mathbf{r}) \nabla_z u_z(\mathbf{r}) \nabla_z u_z(\mathbf{r}') \rangle_c, \\ \bar{\mathcal{T}}_{5,ab} &= -j_1^2 \int d^3\mathbf{x} e^{i\mathbf{k}\cdot\mathbf{x}} \langle u_z(\mathbf{r}') u_z(\mathbf{r}) \delta(\mathbf{r}) \delta(\mathbf{r}') \rangle_c b_{a1} b_{b1}, \\ \bar{\mathcal{T}}_{6,ab} &= -2j_1^2 \int d^3\mathbf{x} e^{i\mathbf{k}\cdot\mathbf{x}} \langle u_z(\mathbf{r}') u_z(\mathbf{r}) \delta(\mathbf{r}) \nabla_z u_z(\mathbf{r}') \rangle_c (b_{a1} + b_{b1}), \\ \bar{\mathcal{T}}_{7,ab} &= -j_1^2 \int d^3\mathbf{x} e^{i\mathbf{k}\cdot\mathbf{x}} \langle u_z(\mathbf{r}') u_z(\mathbf{r}) \nabla_z u_z(\mathbf{r}) \nabla_z u_z(\mathbf{r}') \rangle_c.\end{aligned}\quad (\text{B13})$$

and rescaled with respect to the barred quantity in fiducial cosmology with the growth functions, which leads to the following prediction in general cosmology:

$$\begin{aligned}T(k, \mu) &= \sum_{n=1}^7 \mathcal{T}_{n,ab} = (G_\delta/\bar{G}_\delta)^2 (G_\Theta/\bar{G}_\Theta)^2 \bar{\mathcal{T}}_{1,ab} \\ &\quad + (G_\delta/\bar{G}_\delta) (G_\Theta/\bar{G}_\Theta)^3 \bar{\mathcal{T}}_{2,ab} + (G_\delta/\bar{G}_\delta) (G_\Theta/\bar{G}_\Theta)^3 \bar{\mathcal{T}}_{3,ab} \\ &\quad + (G_\Theta/\bar{G}_\Theta)^4 \bar{\mathcal{T}}_{4,ab} + (G_\delta/\bar{G}_\delta)^2 (G_\Theta/\bar{G}_\Theta)^2 \bar{\mathcal{T}}_{5,ab} \\ &\quad + (G_\delta/\bar{G}_\delta) (G_\Theta/\bar{G}_\Theta)^3 \bar{\mathcal{T}}_{6,ab} + (G_\Theta/\bar{G}_\Theta)^4 \bar{\mathcal{T}}_{7,ab}.\end{aligned}\quad (\text{B14})$$

Lastly, the explicit expression for $F_{ab}(k, \mu)$

$$\begin{aligned}F_{ab}(k, \mu) &= -j_1^2 \int d^3\mathbf{x} e^{i\mathbf{k}\cdot\mathbf{x}} \langle u_z u'_z \rangle_c \langle A_2^a A_3^b \rangle_c \\ &= -j_1^2 \int d^3\mathbf{x} e^{i\mathbf{k}\cdot\mathbf{x}} \langle u_z u'_z \rangle_c \langle (b_{a1}\delta + \nabla_z u_z)(b_{b1}\delta' + \nabla_z u'_z) \rangle_c\end{aligned}$$

can be decomposed in fiducial cosmology into three pieces

$$\bar{F}_{ab}(k, \mu) = \sum_{n=1}^3 \bar{\mathcal{F}}_{n,ab},$$

where the explicit forms of $\bar{\mathcal{F}}_{n,ab}$ are given below:

$$\begin{aligned}\bar{\mathcal{F}}_{1,ab} &= -j_1^2 \int d^3x e^{i\mathbf{k}\cdot\mathbf{x}} \langle u_z u'_z \rangle_c \langle \delta(\mathbf{r}) \delta(\mathbf{r}') \rangle_c b_{a1} b_{b1}, \\ \bar{\mathcal{F}}_{2,ab} &= -j_1^2 \int d^3x e^{i\mathbf{k}\cdot\mathbf{x}} \langle u_z u'_z \rangle_c \langle \delta(\mathbf{r}) \nabla_z u_z(\mathbf{r}') \rangle_c (b_{a1} + b_{b1}), \\ \bar{\mathcal{F}}_{3,ab} &= -j_1^2 \int d^3x e^{i\mathbf{k}\cdot\mathbf{x}} \langle u_z u'_z \rangle_c \langle \nabla_z u_z(\mathbf{r}) \nabla_z u_z(\mathbf{r}') \rangle_c.\end{aligned}\quad (B15)$$

Thus, F_{ab} term in general cosmological model is expressed as

$$\begin{aligned}F(k, \mu) &= \sum_{n=1}^3 \mathcal{F}_{n,ab} = (G_\delta/\bar{G}_\delta)^2 (G_\Theta/\bar{G}_\Theta)^2 \bar{\mathcal{F}}_{1,ab} \\ &\quad + (G_\delta/\bar{G}_\delta) (G_\Theta/\bar{G}_\Theta)^3 \bar{\mathcal{F}}_{2,ab} + (G_\Theta/\bar{G}_\Theta)^4 \bar{\mathcal{F}}_{3,ab}.\end{aligned}\quad (B16)$$

Here, the quantities $\bar{\mathcal{B}}_{n,ab}$, $\bar{\mathcal{F}}_{n,ab}$, and $\bar{\mathcal{T}}_{n,ab}$ are measured in the fiducial cosmological model. Both σ_8 and $f\sigma_8$ are estimated from the measured growth functions of G_δ and G_Θ .

C. AN ANALYTICAL ESTIMATION OF THE FISHER MATRIX FOR X_{HI} COMPONENT, $F_{X_{\text{HI}} X_{\text{HI}}}$

To better understand the marginalized posteriors of parameters, we calculate the analytical form of the Fisher matrix $F_{\alpha\beta}$:

$$F_{\alpha\beta} = \sum_{k, \mu} \mathcal{F}_{\alpha\beta}(k, \mu), \quad (C17)$$

where

$$\mathcal{F}_{\alpha\beta}(k, \mu) \equiv \sum_{i,j} \frac{\partial P_i(k, \mu)}{\partial \alpha} \left[C_{\tilde{P}_i \tilde{P}_j} \right]^{-1} \frac{\partial P_j(k, \mu)}{\partial \beta}. \quad (C18)$$

We find

$$\begin{aligned}\mathcal{F}_{\alpha\beta}(k, \mu) &= \frac{N_p}{2(P_{gH}^2 - P_{gg}P_{HH}N_gN_H)^2} \left\{ \frac{\partial P_{gg}}{\partial \alpha} \frac{\partial P_{gg}}{\partial \beta} P_{HH}^2 N_H^2 - 2 \frac{\partial P_{gg}}{\partial \alpha} \frac{\partial P_{gH}}{\partial \beta} P_{gH} P_{HH} N_H + \frac{\partial P_{gg}}{\partial \alpha} \frac{\partial P_{HH}}{\partial \beta} P_{gH}^2 \right. \\ &\quad - 2 \frac{\partial P_{gH}}{\partial \alpha} \frac{\partial P_{gg}}{\partial \beta} P_{gH} P_{HH} N_H + 2 \frac{\partial P_{gH}}{\partial \alpha} \frac{\partial P_{gH}}{\partial \beta} (P_{gH}^2 + P_{gg}P_{HH}N_gN_H) - 2 \frac{\partial P_{gH}}{\partial \alpha} \frac{\partial P_{HH}}{\partial \beta} P_{gH} P_{gg} N_g \\ &\quad \left. + \frac{\partial P_{HH}}{\partial \alpha} \frac{\partial P_{gg}}{\partial \beta} P_{gH}^2 - 2 \frac{\partial P_{HH}}{\partial \alpha} \frac{\partial P_{gH}}{\partial \beta} P_{gg} P_{gH} N_g + \frac{\partial P_{HH}}{\partial \alpha} \frac{\partial P_{HH}}{\partial \beta} P_{gg}^2 N_g^2 \right\},\end{aligned}\quad (C19)$$

where we dropped the dependence of power spectrums on k and μ for brevity.

Diagonal terms are relevant to our marginalized posterior estimations, giving a good sanity check through the Cramér-Rao inequality

$$\sigma(\alpha) \geq \frac{1}{\sqrt{F_{\alpha\alpha}}}. \quad (C20)$$

Especially, we have checked the surprisingly high accuracy in the estimated x_{HI} by directly calculating, using Eq. (C19):

$$\begin{aligned}\mathcal{F}_{x_{\text{HI}} x_{\text{HI}}}(k, \mu) &= \frac{N_p}{2(P_{gH}^2 - P_{gg}P_{HH}N_gN_H)^2} \left\{ 2 \left(\frac{\partial P_{gH}}{\partial x_{\text{HI}}} \right)^2 (P_{gH}^2 + P_{gg}P_{HH}N_gN_H) \right. \\ &\quad \left. - 4 \frac{\partial P_{gH}}{\partial x_{\text{HI}}} \frac{\partial P_{HH}}{\partial x_{\text{HI}}} P_{gg} P_{HH} N_g + \left(\frac{\partial P_{HH}}{\partial x_{\text{HI}}} \right)^2 P_{gg}^2 N_g^2 \right\}.\end{aligned}\quad (C21)$$

This sanity check proves that the reported value on $\sigma(x_{\text{HI}})$ in section 3.3 is correct.

REFERENCES

Adame, A. G., Aguilar, J., Ahlen, S., et al. 2025, *JCAP*, 2025, 021, doi: [10.1088/1475-7516/2025/02/021](https://doi.org/10.1088/1475-7516/2025/02/021)

Amiri, M., Bandura, K., Chen, T., et al. 2023, *ApJ*, 947, 16, doi: [10.3847/1538-4357/acb13f](https://doi.org/10.3847/1538-4357/acb13f)

Anderson, C. J., Luciw, N. J., Li, Y. C., et al. 2018, *MNRAS*, 476, 3382, doi: [10.1093/mnras/sty346](https://doi.org/10.1093/mnras/sty346)

Appleby, S., Tonegawa, M., Park, C., et al. 2023, arXiv e-prints, arXiv:2305.01943, doi: [10.48550/arXiv.2305.01943](https://doi.org/10.48550/arXiv.2305.01943)

Chang, T.-C., Pen, U.-L., Bandura, K., & Peterson, J. B. 2010, *Nature*, 466, 463, doi: [10.1038/nature09187](https://doi.org/10.1038/nature09187)

Chen, Q., Meyer, M., Popping, A., et al. 2021, *MNRAS*, 508, 2758, doi: [10.1093/mnras/stab2810](https://doi.org/10.1093/mnras/stab2810)

CHIME Collaboration, Amiri, M., Bandura, K., et al. 2025, arXiv e-prints, arXiv:2511.19620, doi: [10.48550/arXiv.2511.19620](https://doi.org/10.48550/arXiv.2511.19620)

Chowdhury, A., Kanekar, N., Chengalur, J. N., Sethi, S., & Dwarakanath, K. S. 2020, *Nature*, 586, 369, doi: [10.1038/s41586-020-2794-7](https://doi.org/10.1038/s41586-020-2794-7)

Cunnington, S., Li, Y., Santos, M. G., et al. 2022, *Monthly Notices of the Royal Astronomical Society*, 518, 6262, doi: [10.1093/mnras/stac3060](https://doi.org/10.1093/mnras/stac3060)

Delhaize, J., Meyer, M. J., Staveley-Smith, L., & Boyle, B. J. 2013, *MNRAS*, 433, 1398, doi: [10.1093/mnras/stt810](https://doi.org/10.1093/mnras/stt810)

DESI Collaboration, Aghamousa, A., Aguilar, J., et al. 2016, arXiv e-prints, arXiv:1611.00036, doi: [10.48550/arXiv.1611.00036](https://doi.org/10.48550/arXiv.1611.00036)

Dong, F., Park, C., Hong, S. E., et al. 2023, *ApJ*, 953, 98, doi: [10.3847/1538-4357/acd185](https://doi.org/10.3847/1538-4357/acd185)

Gil-Marín, H., Noreña, J., Verde, L., et al. 2015, *Monthly Notices of the Royal Astronomical Society*, 451, 539, doi: [10.1093/mnras/stv961](https://doi.org/10.1093/mnras/stv961)

Grasha, K., Darling, J., Leroy, A. K., & Bolatto, A. D. 2020, *MNRAS*, 498, 883, doi: [10.1093/mnras/staa2521](https://doi.org/10.1093/mnras/staa2521)

Jones, M. G., Haynes, M. P., Giovanelli, R., & Moorman, C. 2018, *MNRAS*, 477, 2, doi: [10.1093/mnras/sty521](https://doi.org/10.1093/mnras/sty521)

Li, L.-C., Staveley-Smith, L., & Rhee, J. 2021, *Research in Astronomy and Astrophysics*, 21, 030, doi: [10.1088/1674-4527/21/2/30](https://doi.org/10.1088/1674-4527/21/2/30)

Liu, A., Parsons, A. R., & Trott, C. M. 2014, *Phys. Rev. D*, 90, 023018, doi: [10.1103/PhysRevD.90.023018](https://doi.org/10.1103/PhysRevD.90.023018)

Masui, K. W., Switzer, E. R., Banavar, N., et al. 2013, *ApJL*, 763, L20, doi: [10.1088/2041-8205/763/1/L20](https://doi.org/10.1088/2041-8205/763/1/L20)

McDonald, P., & Roy, A. 2009, *Journal of Cosmology and Astroparticle Physics*, 2009, 020, doi: [10.1088/1475-7516/2009/08/020](https://doi.org/10.1088/1475-7516/2009/08/020)

Pen, U.-L., Staveley-Smith, L., Peterson, J. B., & Chang, T.-C. 2009, *MNRAS*, 394, L6, doi: [10.1111/j.1745-3933.2008.00581.x](https://doi.org/10.1111/j.1745-3933.2008.00581.x)

Planck Collaboration, Ade, P. A. R., Aghanim, N., et al. 2016, *A&A*, 594, A13, doi: [10.1051/0004-6361/201525830](https://doi.org/10.1051/0004-6361/201525830)

Rao, S. M., Turnshek, D. A., & Nestor, D. B. 2006, *ApJ*, 636, 610, doi: [10.1086/498132](https://doi.org/10.1086/498132)

Rhee, J., Lah, P., Briggs, F. H., et al. 2018, *MNRAS*, 473, 1879, doi: [10.1093/mnras/stx2461](https://doi.org/10.1093/mnras/stx2461)

Rhee, J., Zwaan, M. A., Briggs, F. H., et al. 2013, *MNRAS*, 435, 2693, doi: [10.1093/mnras/stt1481](https://doi.org/10.1093/mnras/stt1481)

Saito, S., Baldauf, T., Vlah, Z., et al. 2014, *Phys. Rev. D*, 90, 123522, doi: [10.1103/PhysRevD.90.123522](https://doi.org/10.1103/PhysRevD.90.123522)

Seo, H.-J., Dodelson, S., Marriner, J., et al. 2010, *The Astrophysical Journal*, 721, 164, doi: [10.1088/0004-637X/721/1/164](https://doi.org/10.1088/0004-637X/721/1/164)

Shi, F., Song, Y.-S., Asorey, J., et al. 2020, *Monthly Notices of the Royal Astronomical Society*, 499, 4613, doi: [10.1093/mnras/staa2914](https://doi.org/10.1093/mnras/staa2914)

Song, Y.-S., Taruya, A., & Oka, A. 2015, *JCAP*, 2015, 007, doi: [10.1088/1475-7516/2015/08/007](https://doi.org/10.1088/1475-7516/2015/08/007)

Song, Y.-S., Zheng, Y., Taruya, A., & Oh, M. 2018, *Journal of Cosmology and Astroparticle Physics*, 2018, 018, doi: [10.1088/1475-7516/2018/07/018](https://doi.org/10.1088/1475-7516/2018/07/018)

Takahashi, R., Sato, M., Nishimichi, T., Taruya, A., & Oguri, M. 2012, *ApJ*, 761, 152, doi: [10.1088/0004-637X/761/2/152](https://doi.org/10.1088/0004-637X/761/2/152)

Taruya, A., Bernardeau, F., Nishimichi, T., & Codis, S. 2012, *PhRvD*, 86, 103528, doi: [10.1103/PhysRevD.86.103528](https://doi.org/10.1103/PhysRevD.86.103528)

Tramonte, D., & Ma, Y.-Z. 2020, *MNRAS*, 498, 5916, doi: [10.1093/mnras/staa2727](https://doi.org/10.1093/mnras/staa2727)

White, M., Song, Y.-S., & Percival, W. J. 2008, *Mon. Not. Roy. Astron. Soc.*, 397, 1348, doi: [10.1111/j.1365-2966.2008.14379.x](https://doi.org/10.1111/j.1365-2966.2008.14379.x)

Wolz, L., Pourtsidou, A., Masui, K. W., et al. 2022, *MNRAS*, 510, 3495, doi: [10.1093/mnras/stab3621](https://doi.org/10.1093/mnras/stab3621)

Zhang, C.-P., Zhu, M., Jiang, P., et al. 2024, *Science China Physics, Mechanics, and Astronomy*, 67, 219511, doi: [10.1007/s11433-023-2219-7](https://doi.org/10.1007/s11433-023-2219-7)

Zheng, Y., & Song, Y.-S. 2016, *Journal of Cosmology and Astroparticle Physics*, 2016, 050, doi: [10.1088/1475-7516/2016/08/050](https://doi.org/10.1088/1475-7516/2016/08/050)

Zheng, Y., Song, Y.-S., & Oh, M. 2019, Journal of Cosmology and Astroparticle Physics, 2019, 013, doi: [10.1088/1475-7516/2019/06/013](https://doi.org/10.1088/1475-7516/2019/06/013)

Zwaan, M. A., Meyer, M. J., Staveley-Smith, L., & Webster, R. L. 2005, MNRAS, 359, L30, doi: [10.1111/j.1745-3933.2005.00029.x](https://doi.org/10.1111/j.1745-3933.2005.00029.x)